

Integrated guidance and control framework for the waypoint navigation of a miniature aircraft with highly coupled longitudinal and lateral dynamics

K Harikumar, Jinraj V. Pushpangathan, Sidhant Dhall, and M. Seetharama Bhat

Abstract

A solution to the waypoint navigation problem for fixed wing micro air vehicles (MAV) is addressed in this paper, in the framework of integrated guidance and control (IGC). IGC yields a single step solution to the waypoint navigation problem, unlike conventional multiple loop design. The pure proportional navigation (PPN) guidance law is integrated with the MAV dynamics. A multivariable static output feedback (SOF) controller is designed for the linear state space model formulated in IGC framework. The waypoint navigation algorithm handles the minimum turn radius constraint of the MAV. The algorithm also evaluates the feasibility of reaching a waypoint. Extensive non-linear simulations are performed on high fidelity 150 mm wingspan MAV model to demonstrate the potential advantages of the proposed waypoint navigation algorithm.

Index Terms

Integrated guidance and control, coupled dynamics, micro air vehicle, static output feedback, waypoint navigation.

K. Harikumar is a Research Fellow @ Singapore University of Technology and Design, Singapore, e-mail: harikumar100@gmail.com,

Jinraj V. Pushpangathan is a Research Fellow @ Department of Aerospace Engineering, Indian Institute of Science, Bangalore, India, e-mail: jinrajaero@gmail.com

Sidhant Dhall is a Research Assistant @ Department of Aerospace Engineering, Indian Institute of Science, Bangalore, India, email: sidhant.dhall@gmail.com

M. Seetharama Bhat is a Professor @ Department of Aerospace Engineering, Indian Institute of Science, Bangalore, India, e-mail: msbdcl@aero.iisc.ernet.in

I. INTRODUCTION

Fixed wing micro air vehicles (MAV) are extremely agile, lightweight aircraft with a maximum wingspan of 150 mm [1]. In any of the MAV applications, it has to reach a set of waypoints, specified by the end user. In most of the waypoint navigation problems, guidance and control are treated as two separate problems. Control system is usually designed to give higher bandwidth to track the commands generated by the guidance law. But when the guidance law is integrated with the inner loop control system, the combined system often fails to meet the required performance and stability specifications. The major reasons are due to the assumption of lower order dynamics for the inner loop control system, neglecting actuator bandwidth and assuming decoupled longitudinal and lateral dynamics, especially for the case of MAVs. Many of the guidance law in the literature assumes lower order autopilot for inner loop control system [2]. The assumption of lower order inner loop autopilot provides fictitious high amplitude gain margin for guidance law to operate. When the combined system is not stable, the guidance law parameters are retuned to ensure stability. The re-tuning of guidance law parameters often lead to inadequate performance. The actuator bandwidth is of major concern for MAVs. The short period mode and Dutch roll mode natural frequencies of MAVs are comparable to actuator bandwidth [3]. The relatively lower actuator bandwidth in MAVs leads to poor wind disturbance rejection. The wind disturbances change angle of attack (α) and side slip angle (β) considerably from the trim operating conditions. The additional forces and moments generated by wind disturbances are often neglected while designing the guidance law in the presence of wind [4]. The coupling between longitudinal and lateral dynamics is severe for MAVs and cannot be neglected as in the case of bigger UAVs [3],[5]. The guidance law design needs to consider the combined longitudinal and lateral dynamics, failure of which leads to instability during abrupt maneuvers. The topic of integrated guidance and control (IGC) has gained considerable interest in the area of missile guidance and control [6]-[11] due to the following advantages. The synergy between the guidance and control subsystems can be exploited to make the combined system more stable and effective than the individual subsystems [6]. Despite the fact that separate guidance and control has been applied successfully, still there remains scope for further optimizing the performance and enhancing the stability [7]. The prime focus on the missile IGC design is to achieve improved terminal miss distances. When the missile approaches the target, the time scale separation between the control loop and guidance loop is no longer valid [8]. The conventional

approach of designing separate guidance and control leads to a conservative design with the requirement of actuators with higher bandwidth than necessary [9].

The idea of IGC is also applied to fixed wing UAVs [12]-[16]. A linear time invariant model in the framework of integrated guidance and control is developed for a fixed wing UAV of wingspan 3.8 m to track helical trim trajectories in [12]. For a UAV flying along the trim trajectory, the net forces and moments acting on the UAV are zero. The method developed in [12] explains how to follow a given helical trajectory in which UAV remains in a trimmed state. But finding such a trimmed trajectory connecting two waypoints is very computationally intensive. Moreover, the method cannot be applied for in-flight waypoint changes since it is difficult to compute the trim trajectories online with the limited onboard computational power available with MAV. The IGC design for a fixed wing UAV of 8.8 m wingspan for following a predefined path using sliding mode control is explained in [13]. The design assumes that the roll, pitch and yaw dynamics are decoupled. But for MAVs, the roll, pitch and yaw dynamics are tightly coupled [5]. Nonlinear dynamic inversion (NDI) based IGC framework is developed for UAVs in [14] and [15]. NDI utilizes full state feedback structure. In the case of MAVs, measurement of α and β is tedious due to the lack of availability of lightweight sensors. Moreover, the perturbations in α and β are very high for the MAVs when compared to bigger UAVs under nominal wind conditions. IGC framework developed for lateral dynamics of a fixed wing UAV assumes decoupled longitudinal dynamics in [16]. But the assumptions of decoupled longitudinal and lateral dynamics is not valid for 150 mm class of MAVs [3],[5].

To overcome the above-mentioned limitations of existing IGC methodology, a novel IGC framework is derived in this paper, combining the idea of pure proportional navigation (PPN) with MAV dynamics. The proposed waypoint navigation algorithm based on IGC framework is non-iterative and hence computationally inexpensive. The issue of coupling between longitudinal and lateral dynamics of the MAV is handled by the proposed IGC framework. Unlike the existing algorithms based on IGC framework, the proposed waypoint navigation algorithm evaluates the feasibility of reaching a waypoint based on the acceleration constraints of the MAV. A H_∞ SOF controller is designed for the combined guidance and control loop using Linear Matrix Inequality (LMI) techniques. Numerical simulation results are presented for the straight line following and rectangular path following using high fidelity nonlinear model of a MAV obtained from wind tunnel data.

The paper is organized as follows. The coupled linear state space model of the MAV is presented

in section II. The guidance law used in IGC framework is given in section III. The integration of guidance law to the coupled dynamics of MAV and the waypoint navigation algorithm is presented in section IV. The non-linear six degrees of freedom simulations for straight line following and rectangular path following is given in section V, followed by conclusions.

II. PRELIMINARIES

A. Coupled linear state space model of the MAV

The specifications of the MAV considered in this paper is given in Table I, [1], [5].

TABLE I
SPECIFICATIONS OF THE MAV

Planform	Rectangular
Take-off weight	53 grams
Cruise airspeed	8 <i>m/s</i>
Stall airspeed	6 <i>m/s</i>
Wing - chord length	0.11 <i>m</i>
Wing - span length	0.15 <i>m</i>
Airfoil	E387
Control surfaces	Elevator and rudder

The coupling between longitudinal and lateral dynamics is severe for the case of MAVs. The coupled linear state space shows an unstable spiral mode, whereas the decoupled model fails to capture the unstable spiral mode [5]. The effects of asymmetric propeller wake, motor-propeller counter torque and gyroscopic effects lead to unstable spiral mode dynamics [5], [17]. The coupled linear state space model of the MAV is given in (1).

$$\dot{X} = A_c X + B_c U \quad (1)$$

where

$$X = [\tilde{u}, \tilde{w}, \tilde{q}, \tilde{\theta}, \tilde{h}, \tilde{v}, \tilde{p}, \tilde{r}, \tilde{\phi}]^T \quad (2)$$

and

$$U = [\tilde{\delta}_{es}, \tilde{\delta}_{rs}, \tilde{\delta}_t]^T \quad (3)$$

The set $(\tilde{u}, \tilde{v}, \tilde{w})$ represents the linearized velocity along body axis, $(\tilde{p}, \tilde{q}, \tilde{r})$ are the linearized angular rates, $\tilde{\phi}$ is the linearized roll angle, $\tilde{\theta}$ is the linearized pitch angle and \tilde{h} is the linearized

altitude. The linearized elevator servo output $\tilde{\delta}_{es}$, linearized rudder servo output $\tilde{\delta}_{rs}$ and the linearized thrust generated by motor-propeller denoted by $\tilde{\delta}_t$ are the control inputs. A_c is the system matrix for coupled state space model and B_c is the input matrix. The matrices A_c and B_c are given in [5] for the case of 150 mm wingspan fixed wing MAV.

The states of longitudinal dynamics is given by

$$X_1 = [\tilde{u}, \tilde{w}, \tilde{q}, \tilde{\theta}, \tilde{h}]^T \quad (4)$$

Similarly, the states of lateral dynamics is given by

$$X_2 = [\tilde{v}, \tilde{p}, \tilde{r}, \tilde{\phi}]^T \quad (5)$$

The matrix A_c in (1) can be written as

$$A_c = \begin{pmatrix} A_{11} & A_{12} \\ A_{21} & A_{22} \end{pmatrix} \quad (6)$$

where A_{11} denotes the state matrix for decoupled longitudinal dynamics and A_{22} the state matrix for decoupled lateral dynamics. The coupling between longitudinal and lateral dynamics is introduced by the matrices A_{12} and A_{21} . For bigger UAVs, the eigenvalues of A_c denoted by $\bar{\lambda}(A_c) = \bar{\lambda}(A_{11}) \cup \bar{\lambda}(A_{22})$. But for the case of 150 mm wingspan MAVs, $\bar{\lambda}(A_c) \neq \bar{\lambda}(A_{11}) \cup \bar{\lambda}(A_{22})$ [5].

Remark: In the rest of this paper, a variable with $\tilde{\cdot}$ symbol denotes the linearized variable. For example, the variables (u, v, w) denotes the velocity components along the body axis and $(\tilde{u}, \tilde{v}, \tilde{w})$ represents their linearized version.

III. GUIDANCE LOGIC FOR WAYPOINT NAVIGATION IN TWO DIMENSIONAL SPACE

The origin of the local inertial coordinate system $(X_I Y_I Z_I)$ is the home location of the MAV as shown in Fig. 1 with positive X_I axis towards the geographic north pole, positive Y_I axis in the direction of 90° clockwise rotation from positive X_I axis and positive Z_I axis points towards the down direction. For the waypoint following in 2D space, altitude hold is employed using altimeter feedback, so motion in the local inertial $X_I Y_I$ plane is only considered. The guidance logic is explained first in this section and the integration of the guidance logic with the control system is explained later in section IV.

In Fig. 2, axes $X'Y'$ are parallel to $X_I Y_I$, (x, y) is the current MAV position in the $X_I Y_I$ plane, (x_f, y_f) is the next waypoint to be followed, r_a is the range, σ is the angle between the line

joining (x, y) , (x_f, y_f) and the Y' axis, χ is the angle made by the velocity vector with the X' axis. The miss distance d is the perpendicular distance between (x_f, y_f) and the velocity vector. The applied acceleration is denoted by a_c and is perpendicular to the velocity vector and lies in the $X_I Y_I$ plane. The units of (x, y) , (x_f, y_f) , d , r_a are in meters (m), V_a is in meters/second (m/s), a_c is in meters/second-square(m/s^2) and σ , χ are in radians(rad). From Fig. 2, we can write the following relations given in (7) to (11).

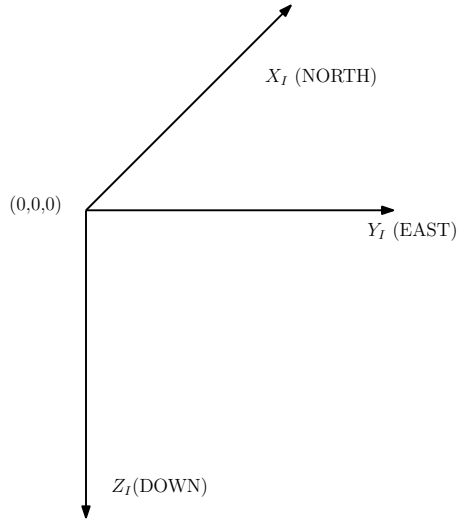


Fig. 1. Diagram showing inertial $X_I Y_I Z_I$ co-ordinate system

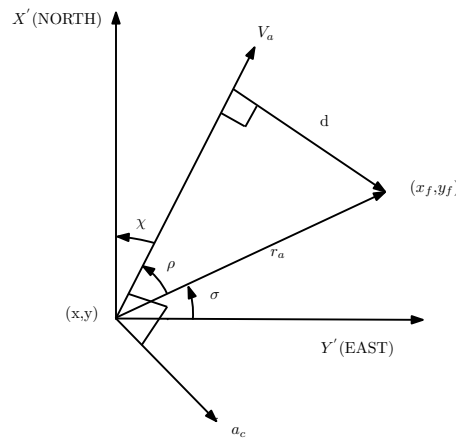


Fig. 2. Diagram explaining the guidance law

$$\sigma = \tan^{-1}\left(\frac{x_f - x}{y_f - y}\right) \quad (7)$$

$$\rho = \frac{\pi}{2} - (\chi + \sigma) \quad (8)$$

$$r_a = \sqrt{(x_f - x)^2 + (y_f - y)^2} \quad (9)$$

$$d = r_a \sin \rho \quad (10)$$

$$a_c = k_1 d \quad (11)$$

In (11), k_1 is the proportional gain. The magnitude of applied acceleration depends upon k_1 . An expression for the gain k_1 is given in the subsection III-A. The acceleration is applied perpendicular to the velocity vector in such a way that it does not change the magnitude of velocity but only the direction. This is analogous to Pure Proportional Navigation (PPN) where the acceleration applied is perpendicular to the velocity vector [19]. Here it is assumed that altitude and V_a is constant. When the miss distance is zero, from (10), we obtain either $r_a = 0$ or $\rho = 0$. The condition $r_a = 0$ implies that $x = x_f$ and $y = y_f$. From Fig. 2, $\rho = 0$ implies that the velocity vector is pointing towards the goal point. So when the miss distance is zero, the MAV has either reached the desired waypoint or the velocity vector of the MAV is along the line connecting the waypoint and current MAV position such that no further acceleration has to be applied to change the direction of the MAV.

A. Relation to PPN Guidance Law and choice of gain k_1

This subsection gives the relation between the proposed guidance law given in (11) and the Pure Proportional Navigation (PPN) guidance law. Consider Fig. 3, in which a_{ppn} denotes the acceleration applied in PPN guidance law and rest all variables are same as in Fig. 2. The expression for PPN guidance law [19] is given by

$$a_{ppn} = -NV_a \dot{\sigma} \quad (12)$$

where $\dot{\sigma}$ is the line of sight rate and N is the navigation constant.

$$\dot{\sigma} = -\frac{V_a \sin \rho}{r_a} \quad (13)$$

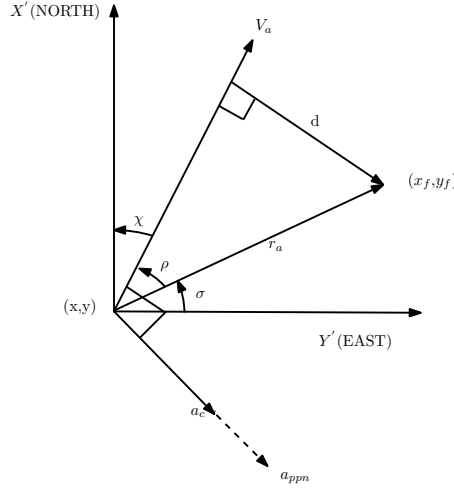


Fig. 3. Diagram used for explaining the relation between the proposed guidance law and PPN guidance law

Using (12) to (13),

$$a_{ppn} = NV_a \left(\frac{V_a \sin \rho}{r_a} \right) \quad (14)$$

From (10) and (11),

$$a_c = k_1 r_a \sin \rho \quad (15)$$

Substituting (15) into (14) gives,

$$a_{ppn} = \left(\frac{N}{k_1} \right) \left(\frac{V_a}{r_a} \right)^2 a_c \quad (16)$$

If we choose k_1 as given in (17), the proposed guidance law is same as the PPN guidance law and is optimal for $N=3$ as shown in [20].

$$k_1 = \frac{N(V_a)^2}{r_a^2} \quad (17)$$

Thus the guidance law given in (11) takes the form

$$a_c = \left(\frac{N(V_a)^2}{r_a^2} \right) d \quad (18)$$

and is same as the PPN guidance law. The guidance law given in (18) will ensure that the MAV will reach the waypoint for $N \geq 2$, [19].

B. Constraint on minimum turn radius

Micro air vehicles have a constraint on the minimum allowable turn radius. The minimum value of the turn radius denoted by R_{min} depends upon the airspeed, stall angle of attack and the maximum thrust available. Since the applied acceleration is perpendicular to the velocity vector, the MAV follows a circular path with an instantaneous radius of curvature inversely proportional to the magnitude of the applied acceleration. The constraint on the applied acceleration a_c can be given as [21]

$$a_c < \frac{V_a^2}{R_{min}} \quad (19)$$

Using (18) and (10), (19) can be written as

$$\left(\frac{N(V_a)^2}{r_a^2}\right)(r_a \sin \rho) < \frac{V_a^2}{R_{min}} \quad (20)$$

After simplifying, (20) becomes

$$\frac{N \sin \rho}{r_a} < \frac{1}{R_{min}} \quad (21)$$

The minimum value for $N = 2$. Hence (21) becomes,

$$r_a > 2R_{min} \sin \rho \quad (22)$$

At any instant, the relation given by (22) ensures that the minimum turn radius constraint is not violated. A waypoint is considered to be not feasible if the condition given in (22) is violated.

IV. INTEGRATED GUIDANCE AND CONTROL FOR WAYPOINT NAVIGATION IN TWO DIMENSIONAL SPACE

In separate guidance and control, the input to the actuator is computed in two sequential stages from the navigation data. Whereas in integrated guidance and control, the input to the actuator is computed in a single step from the navigation data. The block diagram of integrated guidance and control (IGC) is given in Fig. 4. The integrated guidance and control block generates the actuator input (U_I) based on the output (Y_I) and the next waypoint position (x_n, y_n). U_P is the actuator output that deflects the elevator, rudder control surfaces and also changes the thrust input.

The measured output Y_I is given by

$$Y_I = [q, \theta, h, p, r, \phi, d]^T \quad (23)$$

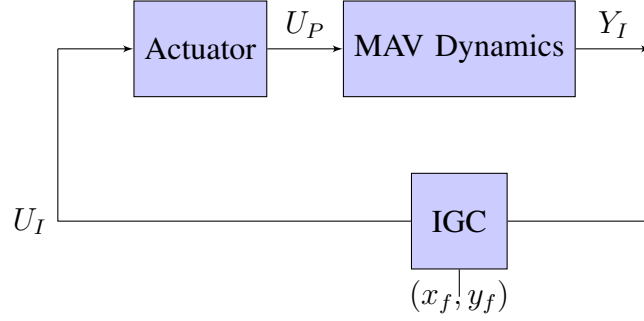


Fig. 4. Architecture of integrated guidance and control for MAV

The yaw angle ψ , the current position of the MAV (x, y) and the next waypoint position (x_f, y_f) is used for the computation of the miss distance d as given in (7) to (10). Here the heading angle $\chi \approx \psi$ assuming the angle of side slip (β) to be small. Let $x_1 = d$, and $\dot{x}_1 = \dot{d} = x_2$. The state variables used in the linear state space model of integrated guidance and control logic are

$$X_I = [X, X_g, X_a]^T \quad (24)$$

where X is given in (2), $X_g = [\tilde{x}_1, \tilde{x}_2]$ are the states corresponding to the guidance logic and $X_a = [\tilde{\delta}_{ep}, \tilde{\delta}_{ep1}, \tilde{\delta}_{er}, \tilde{\delta}_{er1}]$ corresponds to second order elevator and rudder servo actuator transfer function. Thus

$$X_I = [\tilde{u}, \tilde{w}, \tilde{q}, \tilde{\theta}, \tilde{h}, \tilde{v}, \tilde{p}, \tilde{r}, \tilde{\phi}, \tilde{x}_1, \tilde{x}_2, \tilde{\delta}_{ep}, \tilde{\delta}_{ep1}, \tilde{\delta}_{er}, \tilde{\delta}_{er1}]^T \quad (25)$$

In (25), \tilde{x}_1, \tilde{x}_2 are the variables obtained through the linearization of x_1 and x_2 . The first step in the linearization process is to find a relation between $\ddot{x}_2(\ddot{d})$ and the acceleration command a_c . The second step is to find relation between a_c and the turn rate of the vehicle which is a function of $\dot{\psi}$ and $\dot{\beta}$. These two steps will lead to the integration of $X_g = [\tilde{x}_1, \tilde{x}_2]$ to the state vector X to form X_I , since $\dot{\psi}$ and $\dot{\beta}$ is a function of X . As a first step, the commanded acceleration is simplified and is valid for small angles of ρ as given in the below theorem.

Theorem 1: For small angle ρ , the commanded acceleration can be written as

$$a_c = \frac{1}{N-1} \ddot{d} \quad (26)$$

Proof: The approximations $\sin \rho = \rho$ and $\cos \rho = 1$ are done for small angle ρ . From (10),

$$d = r_a \rho \quad (27)$$

Differentiating the above equation gives the following,

$$\dot{d} = \dot{r}_a \rho + r_a \dot{\rho} \quad (28)$$

From (9),

$$\dot{r}_a = -V_a \quad (29)$$

From (8),

$$\dot{\rho} = -\dot{\chi} - \dot{\sigma} \quad (30)$$

Using the relation $a_c = V_a \dot{\chi}$ and from (18)

$$\dot{\chi} = \frac{NV_a d}{r_a^2} \quad (31)$$

From (13) and (10) we obtain,

$$\dot{\sigma} = -\frac{V_a d}{r_a^2} \quad (32)$$

Substituting (31) and (32) into (30) gives,

$$\dot{\rho} = -(N-1) \frac{V_a d}{r_a^2} \quad (33)$$

From (29), (33) and (28) we obtain,

$$\dot{d} = -\frac{NV_a d}{r_a} \quad (34)$$

Differentiating the above equation and using (10) gives,

$$\ddot{d} = -NV_a \frac{d}{dt}(\rho) \quad (35)$$

Using (31) and (32), (35) can be rewritten as

$$\ddot{d} = (N-1) \frac{NV_a^2 d}{r_a^2} \quad (36)$$

Noting that $a_c = \frac{NV_a^2 d}{r_a^2}$, the desired result is obtained.

The approximation of the non-linear guidance law that is valid for small angles of ρ is given in (26). Now as the second step to enable the linearization process, a relationship between a_c and $\dot{\psi}$, $\dot{\beta}$ is derived. In Fig. 5, $X'Y'$ is the body fixed lateral inertial plane of the MAV with X' pointing towards north and Y' pointing towards east, X_B denotes the body X axis, β is the sideslip angle, ψ is the yaw angle. The origin of the body fixed lateral inertial plane is the current position of the MAV denoted by (x, y) . When an acceleration a_c is applied perpendicular

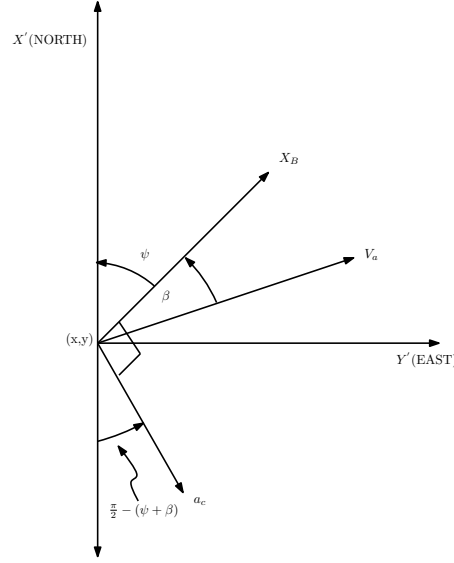


Fig. 5. Body fixed lateral inertial plane of the MAV

to the velocity vector in the yaw plane as shown in the Fig. 5, the MAV will move in a circular path in the body fixed lateral inertial plane with an angular velocity $\dot{\psi} + \dot{\beta}$. Then the applied acceleration can be equated to $V_a(\dot{\psi} + \dot{\beta})$ as given in (37). The heading angle $\chi = \psi + \beta$. From the Fig. 5, we obtain

$$a_c = V_a(\dot{\psi} + \dot{\beta}) \quad (37)$$

The expression for $\dot{\psi}$ and $\dot{\beta}$ is given in (38) and (39) respectively.

$$\dot{\psi} = q \sin \phi \sec \theta + r \cos \phi \sec \theta \quad (38)$$

$$\dot{\beta} = \frac{1}{V_a} (pw - ru + g \cos \theta \sin \phi + \frac{Y_a}{m}) \quad (39)$$

where Y_a is the side-force given by

$$Y_a = \bar{Q} S C_y \quad (40)$$

where $\bar{Q} = 0.5 \rho_a V_a^2$ is the dynamic pressure in N/m^2 and C_y is the side-force coefficient given by

$$C_y = (C_{y\beta} \beta + C_{yp} (\frac{0.5b}{V_a}) p + C_{yr} (\frac{0.5b}{V_a}) r + C_{y\delta r} \delta_r) \quad (41)$$

where $C_{y\beta}$, C_{yp} , C_{yr} and $C_{y\delta_r}$ denotes the change in side-force coefficient due to β , p , r and δ_r respectively. From (37), (38) and (39) we can see that the applied acceleration a_c is a function of the state variables and the rudder input. Thus the state equations for the guidance logic are

$$\dot{x}_1 = x_2 \quad (42)$$

$$\dot{x}_2 = (N - 1)a_c \quad (43)$$

Equations (42) and (43) are linearized and augmented with the MAV dynamic model to obtain the state space model for integrated guidance and control. Let the linearized variables for x_1 and x_2 be \tilde{x}_1 and \tilde{x}_2 respectively. Then the linear state equation and output equation for the integrated guidance and control for two dimensional space is given by

$$\dot{X}_I = AX_I + BU_I \quad (44)$$

$$Y_I = CX_I \quad (45)$$

where X_I is given in (25) and

$$U_I = [\tilde{\delta}_e, \tilde{\delta}_r, \tilde{\delta}_t]^T \quad (46)$$

$$Y_I = [\tilde{q}, \tilde{\theta}, \tilde{h}, \tilde{p}, \tilde{r}, \tilde{\phi}, \tilde{x}_1]^T \quad (47)$$

A. Controller design for IGC framework

For the trim conditions at $V_a = 8m/s$, $\dot{\psi} = 0.8rad/s$ and climb rate $\dot{h} = 1m/s$, the poles of linear state space model corresponding to IGC framework is given in Table II. The spiral mode is unstable for the open loop system.

TABLE II
POLES OF LINEAR STATE SPACE MODEL - IGC FRAMEWORK

Short period mode (ω_{sp} , ζ_{sp})	35.6 rad/s, 0.285
Phugoid mode (ω_{ph} , ζ_{ph})	1.15 rad/s, 0.219
Dutch roll mode, (ω_{dr} , ζ_{dr})	43.8 rad/s, 0.337
Roll subsidence mode	-2.44
Spiral mode	1.51 (unstable)
Elevator servo (ω_e , ζ_e)	48.7 rad/s, 0.742
Rudder servo (ω_r , ζ_r)	48.7 rad/s, 0.742
Poles for \tilde{h} , \tilde{x}_1 , \tilde{x}_2	0, 0, 0

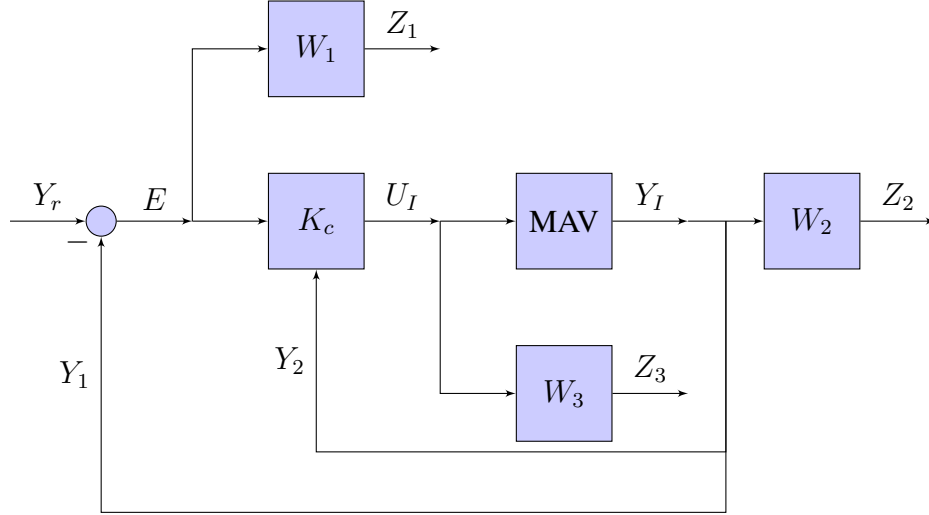


Fig. 6. H_∞ control architecture for IGC framework

The controller is synthesized in H_∞ robust control framework as it can handle uncertainties associated with the MAV dynamics. The architecture of H_∞ control for IGC framework is shown in Fig. 6. Here the reference signal $Y_r = [\tilde{h}_r, \tilde{x}_{1r}]^T$, and the measured outputs $Y_1 = [\tilde{h}, \tilde{x}_1]^T$, $Y_2 = [\tilde{q}, \tilde{\theta}, \tilde{p}, \tilde{r}, \tilde{\phi}]^T$. The weighting transfer functions W_1 , W_2 and W_3 are low pass filter, high pass filter and constant respectively [22]. Z_1 , Z_2 , Z_3 are the performance outputs to be minimized. The controller synthesis is performed in the discrete time domain using the algorithm described in [5]. The controller sampling time is 0.02 seconds (the standard for servo control). The algorithm is summarized as given below. The discrete time equivalent linear state space model of the generalized plant shown in Fig. 6 is given in (48) to (52).

$$X_{dg}(k+1) = A_{dg}X_{dg}(k) + B_{du}U_{dc}(k) + B_{dw}W_{dd}(k) \quad (48)$$

$$Z_{d1}(k) = C_{d1}X_{dg}(k) + D_{d11}U_{dc}(k) + D_{d12}W_{dd}(k) \quad (49)$$

$$Z_{d2}(k) = C_{d2}X_{dg}(k) + D_{d21}U_{dc}(k) + D_{d22}W_{dd}(k) \quad (50)$$

$$Z_{d3}(k) = C_{d3}X_{dg}(k) + D_{d31}U_{dc}(k) + D_{d32}W_{dd}(k) \quad (51)$$

$$Y_d(k) = C_dX_{dg}(k) \quad (52)$$

The controller design objective is to synthesis a SOF control law,

$$U_{dc}(k) = F_dY_d(k) \quad (53)$$

that minimizes the weighted sensitivity, weighted complimentary sensitivity and weighted control input sensitivity function. The gain matrix F_d is obtained by solving the LMI (linear matrix inequality) given in (54). The matrix N_d is selected using the genetic algorithm (GA) for minimizing a performance index considering the closed loop damping ratio and stability of spiral mode and the resultant LMI is solved for P_d and F_d . The matrix $P_d > 0$ for a feasible solution F_d that stabilizes the closed loop plant.

$$\begin{pmatrix} -P_d & -(A_{dg} + B_{du}F_dC_d)^T N_d^T \\ -N_d(A_{dg} + B_{du}F_dC_d) & P_d - N_d - N_d^T \end{pmatrix} < 0 \quad (54)$$

The controller gain matrix F_d is given in (55).

$$F_d = [F_{d1}, F_{d2}] \quad (55)$$

$$F_{d1} = \begin{bmatrix} -0.0060 & -0.3378 & -0.8032 \\ 0 & 0.0987 & 0 \\ -1.152 & 36.54 & 0.0042 \end{bmatrix} \quad (56)$$

$$F_{d2} = \begin{bmatrix} 0.0002 & -0.0007 & 0 & -0.1008 \\ -0.0528 & 0.0008 & -0.0937 & -0.0002 \\ -5.325 & -19.1 & 0.0004 & 0.0091 \end{bmatrix} \quad (57)$$

For the trim conditions at $V_a = 8m/s$, $\dot{\psi} = 0.8rad/s$ and climb rate $\dot{h} = 1m/s$, the dynamic modes of IGC closed loop linear state space model in continuous time domain is given in Table III. From the Table III, we can see that the spiral mode is stabilized and the damping ratio of other modes have improved when compared to open loop plant. The three poles at the origin corresponding to \tilde{h} , \tilde{x}_1 and \tilde{x}_2 are placed in the left half of the s-plane.

B. Waypoint navigation algorithm using IGC framework

Inputs to the algorithm are the current (x, y) position of the MAV obtained from GPS, the desired waypoint position (x_f, y_f) , altitude h obtained from altimeter, rate gyro outputs p, q, r and Euler angles ϕ, θ, ψ . The steps are summarized in *Algorithm I*. For a given waypoint, the angle ρ is computed from (8) and a constant roll angle command is issued if $|\rho| > 20^\circ$. Here the small angle approximation $\sin\rho = \rho$ and $\cos\rho = 1$ is used for $|\rho| \leq 20^\circ$ and the expression given in (26) is valid for the same. The roll angle control for 150 mm MAV given in [3] is used here.

TABLE III
POLES OF CLOSED LOOP IGC LINEAR STATE SPACE MODEL

Short period mode $(\omega_{sp}, \zeta_{sp})$	36.8 rad/s, 0.404
Phugoid mode $(\omega_{ph}, \zeta_{ph})$	2.25 rad/s, 0.323
Dutch roll mode, $(\omega_{dr}, \zeta_{dr})$	30.0 rad/s, 0.429
Roll subsidence mode	-15.5
Spiral mode	-3.24
Pole for \tilde{h}	-1.50
Poles for \tilde{x}_1, \tilde{x}_2 (ω, ζ)	0.1 rad/s, 0.343
Elevator servo (ω_e, ζ_e)	44.4 rad/s, 0.671
Rudder servo (ω_r, ζ_r)	49.5 rad/s, 0.603

The altitude is maintained constant while executing the roll angle command. The MAV follows a constant roll angle command $\phi_{ref} = \text{sgn}(\rho)\phi_r$ for $|\rho| > 20^0$. Here ϕ_r is a constant value less than the maximum allowed roll angle ϕ_{max} of the MAV. When $|\rho| \leq 20^0$, the feasibility of reaching the waypoint is verified using (19) and subsequently the control law given in (53) is employed as the IGC framework is valid. When the range (r_a) is less than a pre-defined threshold r_t , the waypoint is considered to be reached and the entire process is repeated for a new waypoint.

Algorithm I:

STEP I: Compute ρ from (8).

STEP II: **else-if** $|\rho| > 20^0$ Issue a roll angle hold command $\phi_{ref} = \text{sgn}(\rho)\phi_r$, where $0 < \phi_r < \phi_{max}$ and **goto** STEP I.

else-if $r_a > 2R_{min}\sin\rho$ Use the controller structure given in (53) and **goto** STEP III.

Current waypoint is not feasible, **goto** STEP IV.

STEP III: **else-if** $r_a < r_t$ Waypoint reached, **goto** STEP IV **else goto** STEP I.

STEP IV: Switch to a new waypoint and **goto** STEP I.

V. NUMERICAL SIMULATION RESULTS FOR WAYPOINT NAVIGATION

The waypoint navigation algorithm is simulated for the non-linear six degrees of freedom (6DOF) model of the 150 mm MAV given in [1]. Flight test results are presented in [1], validating the non-linear model used for simulation. Two simulations are performed in which the first one is to demonstrate straight line path following and for the second one, the objective is to follow

a rectangular path. Constraints are put on the actuators while performing the simulations. The range of elevator deflection is $[-35^\circ, 15^\circ]$, rudder deflection is $[-25^\circ, 25^\circ]$ and motor thrust is 0.0-0.45 N. The second order transfer function model is used for elevator and rudder servos. The control input update is done at every 0.02 second. The XY position update is done at every 1 second. All other outputs are sampled at a rate of 0.02 second. The waypoint navigation logic is started when the MAV reach at an altitude of 20 m from the ground level. Altitude feedback is used to maintain the desired altitude of 20 m. For both the simulations, the initial conditions are shown in Table IV.

TABLE IV
INITIAL CONDITIONS USED FOR THE NON-LINEAR SIMULATION

Variable	Value
V_a, α, β	8 m/s, 0.2286 rad, -0.0532 rad
$\delta_e, \delta_r, \delta_t$	-0.2592 rad, 0.1255 rad, 0.231 N
ϕ, θ, ψ	-0.0361 rad, 0.2304 rad, 0 rad
p, q, r	0 rad/s, 0 rad/s, 0 rad/s
u, v, w	7.78 m/s, -0.43 m/s, 1.81 m/s
x, y, h	0 m, 0 m, 20 m

The objective of the first simulation is to follow a straight line. The XY (North-East) path of the MAV is shown in Fig. 7. In Fig. 7, red circles represent the waypoints commanded and the solid blue line represents the path followed by the MAV. The plot of miss distance and the angle ρ is given in Fig. 8. During the initial stage, the miss distance is high as the first waypoint is not along the line-of-sight (LOS) of the MAV. After 25 seconds, we can see that the value of ρ and miss distance is closer to zero as the MAV got aligned to the straight line. The small angle approximation used in the derivation of the IGC framework is used for $\rho < 20^\circ$. Initially when $\rho > 20^\circ$ till 1.4 seconds, a constant roll angle command of $\phi_r = 10^\circ$ is employed. A plot of Euler angles and angular rates are given in Fig. 9. The roll angle ϕ goes to 10° as shown in Fig. 9 accordingly. The plot of control inputs is given in Fig. 10. The peak amplitude of elevator deflection is less than -16° and that of the rudder is less than 8° . The peak value of elevator deflection is less than 50% of the saturation value of -35° . The peak value of rudder deflection is less than 33% of the saturation value of 25° . Thus the control inputs are well within the saturation limits. The variation airspeed is between 7.7 m/s and 8.2 m/s as seen from Fig.

10 and is closer to the trim velocity of 8.0 m/s.

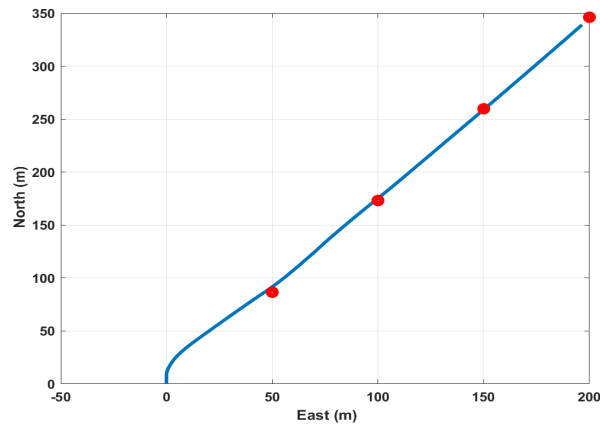


Fig. 7. XY plot for MAV straight line following

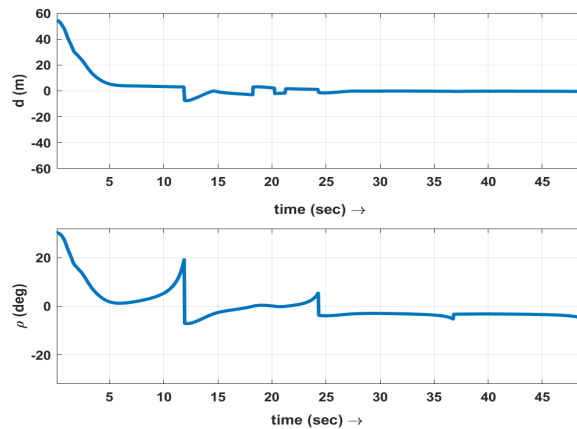


Fig. 8. Miss distance and ρ angle plots for MAV straight line following

The objective of the second simulation is to follow a rectangular path. Following a rectangular path enables the MAV to perform surveillance over a given area. The rectangular path considered is of size 100m x 200m. The path followed by the MAV is shown in Fig. 11. In Fig. 11, small red circles denotes the waypoints along the rectangular path and blue line represents the path followed by the MAV. The starting point of the flight path is at (0,0). The MAV takes a turn after reaching the first waypoint at (80,0). The plot of d and ρ given in Fig. 12 show oscillations whenever MAV switches to a new waypoint. The miss distance goes to zero as the MAV approaches a

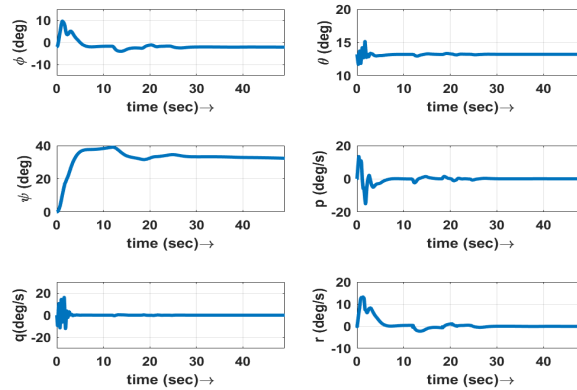


Fig. 9. Euler angles and body axis angular rates for MAV straight line following

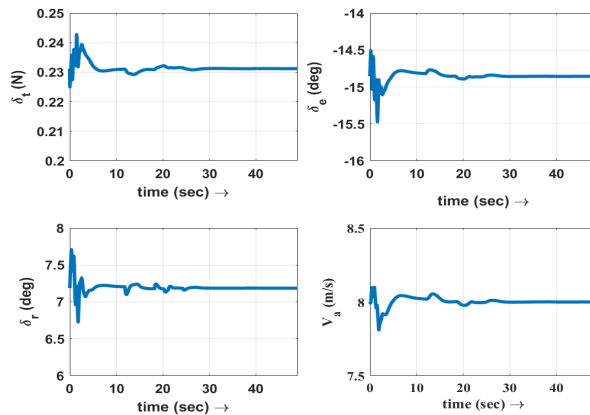


Fig. 10. Control inputs and airspeed for straight line following

waypoint. The plot of control inputs and airspeed for rectangular path following is shown in Fig. 13. The airspeed is between $7\text{--}8.5\text{ m/s}$ for most of the time duration of the MAV flight.

VI. CONCLUSION

The paper presents a novel waypoint navigation algorithm in IGC framework. The IGC methodology combines unstable MAV coupled dynamics with the pure proportional navigation guidance law. The resulting linear closed loop system is found to be stable with a static output feedback control law. The proposed waypoint navigation algorithm handles the minimum turn radius constraint of the MAV and determines the feasibility of reaching a given waypoint. The waypoint

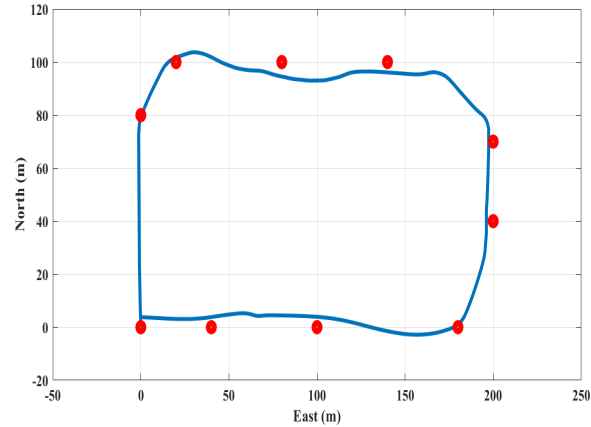


Fig. 11. XY plot for rectangular path following

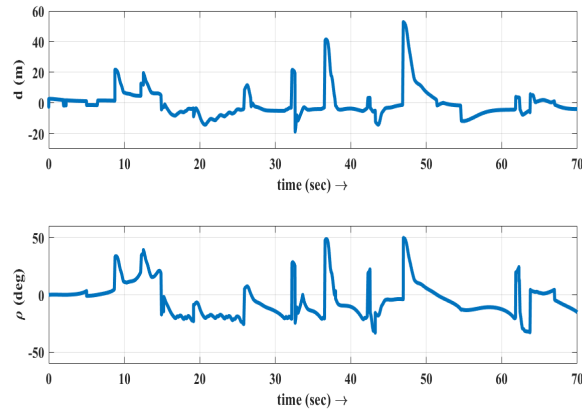


Fig. 12. Miss distance and ρ angle plots for rectangular path following

navigation algorithm does not require any iterative methods to compute the control inputs. The high fidelity nonlinear numerical simulations for straight line and rectangular path following validates the utility of the algorithm. The airspeed of the MAV is maintained well above the stall value while performing the path following. The extension of this algorithm for waypoint navigation in three-dimensional space would be interesting future work.

ACKNOWLEDGMENT

The authors would like to thank National Programme for Micro Air Vehicle (NPMICAV) and Aeronautical Development and Research Board (ARDB), government of India for funding the

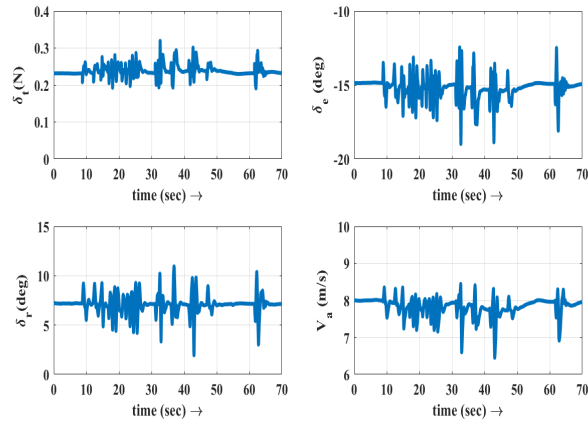


Fig. 13. Control inputs and airspeed for rectangular path following

project.

REFERENCES

- [1] K. Harikumar, J. V. Pushpangathan, T. Bera, S. Dhall, and M. S. Bhat. "Modeling and closed loop flight testing of a fixed wing micro air vehicle," *Micromachines*, Vol. 9, No. 3, p.111, 2018.
- [2] D.R. Nelson, D.B. Barber, T.W. McLain and R.W. Beard, "Vector field path following for miniature air vehicles," *IEEE Transactions on Robotics*, Vol. 23, No. 3, pp. 519-529, 2007.
- [3] K. Harikumar, Sidhant Dhall and M. Seetharama Bhat, "Nonlinear modeling and control of coupled dynamics of a fixed wing micro air vehicle," *Indian Control Conference*, Hyderabad, India, January 2016.
- [4] Sikha Hota and Debasish Ghose, "Time-Optimal Convergence to a Rectilinear Path in the Presence of Wind," *Journal of Intelligent Robotic Systems* Vol. 74, pp. 791-815, 2014.
- [5] K. Harikumar, Sidhant Dhall and M. Seetharama Bhat, "Design and experimental validation of a Robust output feedback control for the coupled dynamics of a micro air vehicle," *Springer International Journal of Control, Automation and Systems*, vol. 17, no. 1, pp. 155-167, 2019.
- [6] H. Yan and H. Ji, "Integrated guidance and control for dual-control missiles based on small-gain theorem," *Automatica* Vol. 48, pp. 2686-2692, 2012.
- [7] M. Xin, S. N. Balakrishnan and E. J. Ohlmeyer, "Integrated Guidance and Control of Missiles With θ - D Method," *IEEE Transactions on Control Systems Technology*, Vol. 14, No. 6, pp. 981-992, 2006.
- [8] Y. Ke, T. Qingke, L. Siyuan, L. Qingdong and R. Zhang, "Integrated guidance and control design based on motion tracking," *Proceedings of the 35th Chinese Control Conference*, Chengdu, China, pp. 5721-5725, 2016.
- [9] P.K. Menon and E.J. Ohlmeyer, "Integrated design of agile missile guidance and autopilot systems," *Control Engineering Practice*, Vol. 9, No. 10, pp. 1095-1106, 2001.
- [10] C. Zhang and W. Yun-jie, "Non-singular terminal dynamic surface control based integrated guidance and control design and simulation," *ISA transactions*, Vol. 63, pp. 112-120, 2016.

- [11] G. Jianguo, Y. Xiong, and J. Zhou, "A new sliding mode control design for integrated missile guidance and control system," *Aerospace Science and Technology*, Vol.78, pp. 54-61, 2018.
- [12] I. Kaminer, A. Pascoal, E. Hallberg and C. Silvestre, "Trajectory tracking for autonomous vehicles: an integrated approach to guidance and control," *Journal of Guidance, Control and Dynamics*, Vol. 21, No. 1, pp. 29-38, 1998.
- [13] T. Yamasaki, S.N. Balakrishnan and H. Takano, "Separate channel integrated guidance and control for automatic path following," *Journal of Guidance, Control and Dynamics*, Vol. 36, No. 1, pp. 25-34, 2013.
- [14] R. Padhi, P. R. Rakesh and R. Venkataraman, "Formation Flying with Nonlinear Partial Integrated Guidance and Control," *IEEE Transactions on Aerospace and Electronic Systems*, Vol. 50, No. 4, pp. 2847-2859, 2014.
- [15] X. Liu, W. Huang, L. Du , P. Lan and Y. Sun, "Three-Dimensional Integrated Guidance and Control for BTT Aircraft Constrained by Terminal Flight Angles, " *27th Chinese Control and Decision Conference (CCDC)*, pp.107-112, 2015.
- [16] M. Z. Babar, R. Samar, A. I. Bhatti and M. Baglietto, "Robust Integrated Lateral Guidance and Control of UAVs," *20th IEEE International Conference on Methods and Models in Automation and Robotics (MMAR)*, pp. 523-528, 2015.
- [17] J. V. Pushpangathan, M. S. Bhat, and K. Harikumar, "Effects of Gyroscopic Coupling and Countertorque in a Fixed-Wing Nano Air Vehicle," *Journal of Aircraft*, vol. 55, no.1, pp. 239-250, 2018.
- [18] J. Roskam, "Airplane design," Part 6, Roskam Aviation and Engineering Corporation, pp. 371-461, 1990.
- [19] N.A. Shneydor, "Missile Guidance and Pursuit: Kinematics, Dynamics and control," Horwood publishing, England, pp. 109-117, 1998.
- [20] R. Yanushevsky, "Guidance of Unmanned Aerial Vehicles," CRC Press, pp. 9-18, 2011.
- [21] J.L. Meriam, L.G. Kraige, "Engineering mechanics - Dynamics," Sixth edition, Wiley India, pp. 55-57, 2008.
- [22] H. Jiankun, C. Bohn and H.R. Lu, "Systematic H_∞ weighting function selection and its application to the real-time control of a vertical take-off aircraft," *Control Engineering Practice*, Vol. 8, No. 3, pp. 241-252, 2000.